

Influence of Propulsion Type on the Near-Wake Evolution of Kinetic and Potential Energy *

Matthew C. Jones¹, Eric G. Paterson²

¹ Rolls-Royce Graduate Fellow, Department of Aerospace and Ocean Engineering, Virginia Polytechnic Institute and State University, Blacksburg, VA, 24061, USA, mattjones@vt.edu

² Department Head and Rolls-Royce Commonwealth Professor of Marine Propulsion, Department of Aerospace and Ocean Engineering, Virginia Polytechnic Institute and State University, Blacksburg, VA, 24061, USA, egp@vt.edu

ABSTRACT

To better understand the influence of swirl on the stratified near-wake of a self-propelled axisymmetric vehicle, three propulsor schemes are considered: a single-propeller, contra-rotating propellers (CRP), and a zero-swirl jet. The propellers are modeled using an actuator-line model in an unsteady Reynolds-Averaged Navier-Stokes simulation. Visualization of vortical structures shows the helical paths of blade-tip vortices from the single propeller as well as the complicated vortical interaction between contra-rotating blades. Comparison of instantaneous and time-averaged fields shows that temporally stationary fields emerge by half of a body-length downstream. Circumferentially-averaged axial velocity profiles show similarities between the single-propeller and CRP in contrast to the jet configuration. Swirl-velocity of the CRP, however, was attenuated in comparison to that of the single-propeller case. Mixed-patch contour maps illustrate the unique temperature distribution of each configuration as a consequence of its swirl profiles. Finally, kinetic and potential energy is integrated along downstream axial planes to reveal key differences between the configurations. The CRP creates less potential energy by reducing swirl that would otherwise persist in the near-wake, as exhibited is the single-propeller wake.

Keywords

actuator-line, near-wake, net-zero-momentum, self-propelled, energy-budget

1 INTRODUCTION

Experiments have shown that propeller-driven wakes evolve from a complex near-wake with discernible propeller-blade features, to a far-wake, in which these features have mixed together to form a nearly-axisymmetric field (Hyun, 1990, Hyun & Patel, 1991). Sirviente & Patel (2000a) show that the near-wake region transitions to the far-wake in roughly twelve initial wake diameters. This transition is defined by Reynolds and Swirl numbers in addition to the propeller- and body-geometry (Felli et al., 2011). The swirling propeller induces helical vortices that are shed from the roots and tips of the individual blades. In the near-wake, these vortices break down, which is a topic

of extensive study (Lucca-Negro & O'Doherty, 2001). Although experiments show the contribution of swirl on various wakes, its role in the evolution from near- to far-wake is still largely unknown (Sirviente & Patel, 2000b). Stratification further plays a role in the long-term evolution of the far-wake (Meunier & Spedding, 2006). Originally studied as a disc-with-center-jet (DWCJ) (Naudascher, 1965) and later with self-propelled axisymmetric bodies, (Lin & Pao, 1974, Schetz & Jakubowski, 1975) the net-zero-momentum wake functions as a theoretical model of a self-propelled marine vehicle. Beyond experiment, the study of self-propelled wakes includes several numerical methods. Ordered by increasing fidelity and computational expense these methods include: panel/lattice methods, actuator models, and fully resolved rotating geometry (Sanderse et al., 2011). Generalized actuator models include the Actuator Disk (AD), Actuator Line (AL), and Actuator Surface (AS) models. Each of these models imposes a body force over a volume in a Computational Fluid Dynamics (CFD) simulation to simulate the effects of propeller on the surrounding flow. Although a fully resolved propeller may offer a more accurate simulation, its computational requirements are often large, so an actuator model provides an alternative (Jones & Paterson, 2016).

In a self-propelled near-wake, the interaction between propeller-driven swirl and stratification results in a thermally-mixed patch. By using contra-rotating propellers of equivalent thrust, the initial swirl profile is modified thereby changing the shape of the mixed patch and reducing its integrated potential energy. Contra-rotating propeller blades add additional complexity to the interaction between root- and tip-vortices and their eventual collapse. These influences on the near-wake may be compared to the nominal case of a uniform, zero-swirl jet-propelled configuration, which results in the smallest change in the potential energy of the mixed patch.

In the present study, the unsteady Reynolds-Averaged Navier-Stokes (URANS) equations are solved to examine the near-wake evolution of a stratified, turbulent, net-zero-momentum propeller wake of the axisymmetric Iowa Body using three different propulsion schemes: single propeller, dual-contra-rotating propellers (CRP), and zero-swirl jet.

The propellers are simulated using the AL model. The Iowa Body hull geometry is used to compare to the non-stratified experiment of Hyun & Patel (1991), which is the only known experiment to have phase-averaged propeller data for this case. Circumferentially- and time-averaged profiles of flow parameters are examined in the near-wake and intermediate region to investigate the influence of a propulsion type on the wake evolution. Comparison is made to the theoretical disc-with-center-jet that is often used in many simulations (Brucker & Sarkar, 2010, Chernykh & Voropayeva, 1999, Hassid, 1980). Results show that compared to the single-propeller configuration, the CRP configuration is more effective at reducing potential and kinetic energy in the wake, and potential energy reductions are similar to that of the zero-swirl jet.

2 APPROACH

2.1 Governing Equations

This problem is defined by the Reynolds-averaged Navier-Stokes (RANS) equations in Boussinesq form with an additional body force term f_i to account for the propeller model.

$$\begin{aligned} \frac{\partial \mathbf{U}}{\partial t} + \mathbf{U} \cdot \nabla \mathbf{U} - \nu \nabla^2 \mathbf{U} &= -\nabla \hat{p} + \nabla \cdot \overline{u'_i u'_j} - \mathbf{g} \frac{\Delta \rho}{\rho_0} + f_i \\ \nabla \cdot \mathbf{U} &= 0 \end{aligned} \quad (1)$$

The equations are written in terms of the non-inertial velocity \mathbf{U} . In the equations, ν is the dynamic viscosity, \mathbf{g} is the acceleration due to gravity, ρ is density, and ρ_0 is the reference density. This formulation includes the piezometric pressure, $\hat{p} = p_d / \rho_0$ where $p_d = p - \rho_0 \mathbf{g} \cdot \mathbf{x}$.

Temperature T and salinity S in the ocean environment are determined through the following transport equations.

$$\frac{\partial T}{\partial t} + \nabla \cdot (\mathbf{U}T) = \nabla \cdot [\kappa_T \nabla T] + \nabla \cdot \overline{u'_i t'}, \quad (2)$$

$$\frac{\partial S}{\partial t} + \nabla \cdot (\mathbf{U}S) = \nabla \cdot [\kappa_S \nabla S] + \nabla \cdot \overline{u'_i s'}. \quad (3)$$

The Reynolds stresses $\overline{u'_i u'_j}$ and turbulent fluxes $\overline{u'_i t'}$ and $\overline{u'_i s'}$ are determined using a linear eddy-viscosity closure model.

$$-\overline{u'_i u'_j} = 2\nu_t S_{ij} - \frac{2}{3}k\delta_{ij} \quad (4)$$

$$-\overline{u'_i t'} = \frac{\nu_t}{\sigma_T} \frac{\partial T}{\partial x_i} \quad (5)$$

$$-\overline{u'_i s'} = \frac{\nu_t}{\sigma_S} \frac{\partial S}{\partial x_i} \quad (6)$$

$$-\overline{\Delta \rho' u'_i} = \frac{\nu_t}{\sigma_\rho} \frac{\partial (\Delta \rho)}{\partial x_i} \quad (7)$$

Turbulence may be modeled using a RANS or hybrid RANS/LES approach. In this case the $k - \omega$ SST turbulence model is chosen to compute the eddy viscosity ν_t due to its ease of implementation and relative strength in computing the attached flow over a body. (Menter, 1994) Production

terms in the $k - \omega$ equations are modified to include buoyancy effects, but in the near-wake they are small in comparison to the production due to shear.

Density is computed by solving the UNESCO seawater equation-of-state (Fofonoff & Millard, 1983). For the given problem, it is appropriate to approximate the secant bulk modulus as constant at sea-level conditions, even though it is a function of salinity, temperature, and pressure. Thus, the secant bulk modulus is $K(S, T, p) = K(0, 20, p_{atm})$ where p_{atm} is atmospheric pressure. Additionally, substituting the hydrostatic pressure for the total pressure, the equation-of-state becomes,

$$\rho(S, T, p) = \frac{\rho(S, T, 0)}{1 - p/K(S, T, p)} \quad (8)$$

$$\begin{aligned} \rho(S, T, 0) &= (a_0 + a_1 T + a_2 T^2 + a_3 T^3 + a_4 T^4 + a_5 T^5) \\ &+ (b_0 + b_1 T + b_2 T^2 + b_3 T^3 + b_4 T^4) S \\ &+ (c_0 + c_1 T + c_2 T^2) S^{3/2} \\ &+ d_0 S^2 \end{aligned} \quad (9)$$

2.2 Kinetic and Potential Energy

The evolution and transfer of energy in the wake is examined in the form of kinetic and potential energy defined as,

$$ke = \frac{1}{2} \rho U^2, \quad pe = -\frac{1}{2} \frac{g}{\partial \rho_0 / \partial z} (\rho - \rho_0)^2 \quad (10)$$

$$KE = \iint_S ke \, dS, \quad PE = \iint_S pe \, dS, \quad (11)$$

The per-unit-volume energy ke , and pe may be integrated over an axial slice of area S in the wake to find per-unit-length energy KE and PE as functions of downstream distance. The potential energy per-unit-volume pe follows the formulation of Holliday & McIntyre (1981).

2.3 Actuator-Line Model

The AL model projects a distributed line of force f_i in the place of each propeller blade,

$$f_i(r) = \frac{F_i}{\varepsilon^3 \pi^{3/2}} \exp \left[-\left(\frac{r}{\varepsilon} \right)^2 \right] \quad (12)$$

where $F_i = L_i + D_i$ is the actuator element force composed of lift L_i and drag D_i . The distance between CFD cell center and actuator point is r , and ε controls the Gaussian width. Troldborg (2008) recommends $\varepsilon \equiv 2\Delta x$ where Δx is the grid spacing at the actuator position, but further considerations can be made (Martinez et al., 2012). For this study $\varepsilon \equiv 4\Delta x$ to avoid numerical instability. Lift and drag are computed from a lookup-table of lift and drag coefficients C_ℓ and C_d as functions of local flow angle of attack α ,

$$L = \frac{1}{2} C_\ell(\alpha) \rho U_{rel}^2 c w, \quad D = \frac{1}{2} C_d(\alpha) \rho U_{rel}^2 c w \quad (13)$$

where ρ is the density, U_{rel} is the local flow speed, c is the chord and w is the width of the actuator section. The

relationship between C_ℓ and C_d with α must be predetermined from experiment, simulation, or theory for each airfoil section. Figure 1 shows the magnitude of the projected per-unit-mass body-force \hat{f}_i on the AL propeller plane of the single-propeller case, non-dimensionalized by $R_p \text{ rps}^2$, where R_p is the propeller radius and rps is the propeller rotations per second.

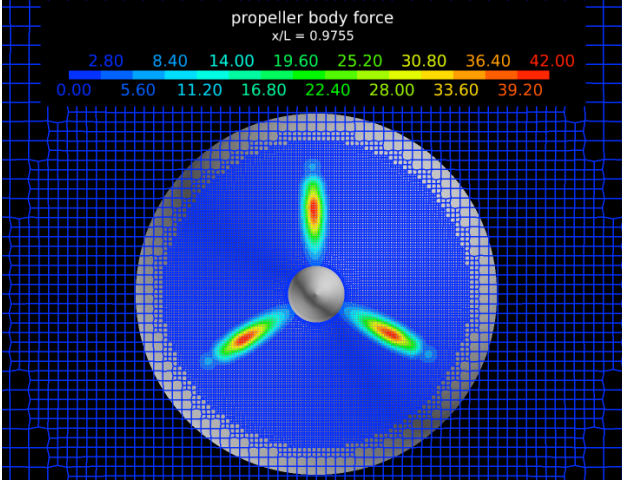


Figure 1: Non-dimensional body force on mesh slice at propeller plane $|\hat{f}_i|/(R_p \text{ rps}^2)$ for the single-propeller case.

2.4 Iowa Body

The Iowa Body, described in the experiment of Hyun & Patel (1991), is shown in Figure 2 as the single-propeller case. This axisymmetric geometry is representative of a typical marine vehicle *without* appendages. Features of this geometry are listed in Table 1 where L is the body length, D is the body diameter, D_p is the propeller diameter, and D_h is the hub diameter.

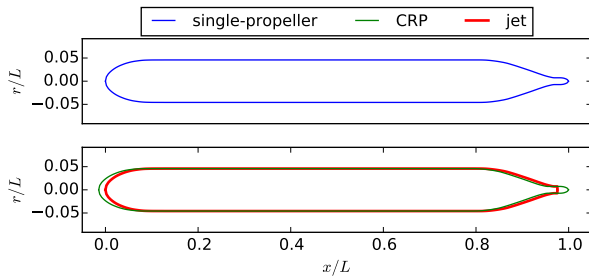


Figure 2: Iowa Body (top) for single-propeller configuration, and extended hull of CRP and truncated hull of jet configuration (bottom).

Table 1: Iowa Body geometry.

Feature	Value
L/D	10.90
D/D_p	1.369
D_p/D_h	6.266
Hub location	$0.9688 < x/L < 0.9832$
Propeller location	$x/L = 0.9755$
Number of blades	3
Propeller airfoil	NACA 66-Modified Airfoil

Modified hulls for the CRP and jet cases are also shown in Figure 2. For the CRP, the hub is extended by the length of the rotating portion so that a second propeller may be placed directly behind the first. For the jet, the hub is cut at the propeller plane to provide for the jet exhaust.

2.5 Iowa Body Propeller

The Iowa Body propeller is defined by 36 discrete sections to account for variations in radial propeller-blade geometry. Sectional lift C_ℓ is computed using the analytic expression of Brockett (1966) for the NACA 66-Modified Airfoil,

$$C_\ell = 2\pi(1 - 0.83\tau)(\alpha + 2.05f) \quad (14)$$

where α is the local flow angle of attack, τ is the maximum thickness ratio, and f is the maximum camber ratio. Sectional drag C_d is imposed by combining viscous and induced drag at each airfoil section,

$$C_d = C_{d0} + \frac{C_\ell^2}{\pi e AR} \quad (15)$$

where C_{d0} is the viscous drag, e is the efficiency factor, and AR is the aspect ratio.

For the given operating conditions the local flow angle of attack typically remains below 2.6° , so these analytic expressions do require conditions for stall. Pitch, chord, thickness, and camber distributions for the Iowa Body propeller blade are tabulated in Hyun (1990). The Iowa Body propeller has zero rake and zero skew.

2.6 Mesh

The computational meshes were generated using the software *cfMesh* from <http://www.cfmesh.com>. Cells are focused near the body, the propeller region, and in the wake. Mesh design and quality features are listed in Table 2.

Table 2: Mesh design and quality features.

Mesh design feature	Value
Boundary layer cells	> 20
Near-wall mesh spacing	$y^+ < 100$
Cells/ D_p (propeller plane/wake region)	100/50
Wake region extends to	$x/L = 1.6$
Total number of cells	$\approx 2 \times 10^7$
Mesh quality feature	Value
Maximum aspect ratio	$AR < 170$
Maximum non-orthogonality	< 45
Maximum skewness	< 0.8

2.7 Flow Field Analysis

This study examines primary flow variables including: change-in-temperature ΔT and the axial, radial, and azimuthal velocities U_x , U_r , and U_θ . Additionally, the following secondary flow variables are examined: Q-criterion visualization; and the integrated energies KE and PE. Data is extracted in axial planes between $0.9755 \leq x/L \leq 1.5$ where x is the downstream distance from the start of the body and L is the body length.

2.8 Flow Coefficients and Case Studies

Several of the important flow coefficients for this propeller-driven flow are Reynolds number Re_L , advance ratio J , thrust coefficient C_T , and torque coefficient C_Q .

$$\begin{aligned} Re_L &= \frac{U_0 L}{\nu}, \quad J = \frac{U_0}{n D_p}, \quad C_T = \frac{\mathcal{T}}{\rho_0 n^2 D_p^4}, \\ C_{T^*} &= \frac{\mathcal{T}}{\frac{1}{2} \rho_0 U_0^2 \pi R_0^2}, \quad C_Q = \frac{Q}{\rho_0 n^2 D_p^5} \end{aligned} \quad (16)$$

For these expressions, ν is kinematic viscosity, D_p is the diameter of the propeller, R_0 is the radius of the Iowa Body, n is the propeller speed in revolutions per second, \mathcal{T} is the thrust, and Q is the torque. \mathcal{T}/\mathcal{D} is the thrust-to-drag ratio. The Reynolds number for this study is $Re_L = 3.1 \times 10^8$, and the other coefficients are listed in Table 3. The fore- and aft-propellers are listed individually for the CRP case, and thrust is equivalent for all cases.

Table 3: Flow coefficients.

Configuration	J	C_T	C_{T^*}	C_Q	\mathcal{T}/\mathcal{D}
Single	0.86	0.047	0.084	0.011	0.99
CRP (fore)	0.90	0.024	0.041	0.0071	0.50
CRP (aft)	0.86	0.023	0.041	0.0072	0.50
Jet	-	-	0.082	0	1.07

The Froude number Fr provides a measure of the density stratification, where $Fr = \infty$ means zero stratification and a small Fr means high levels of stratification. The present study considers a linearly varying temperature stratification with a Froude number of $Fr = 350$, where,

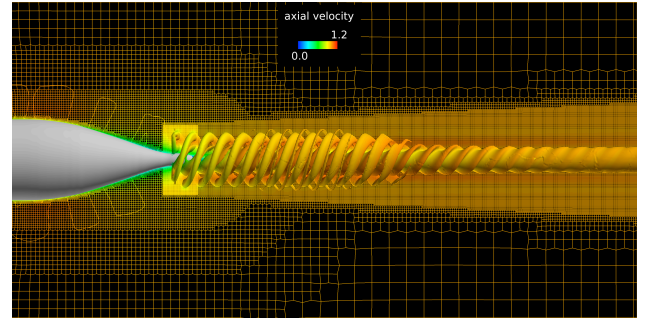
$$Fr = \frac{1}{N} \frac{U_0}{D}, \quad \text{and} \quad N = \frac{1}{2\pi} \sqrt{\frac{-g}{\rho_0} \frac{\partial \rho}{\partial z}}. \quad (17)$$

In these expressions N is the Brunt Väisälä frequency, g is acceleration due to gravity, and z is the vertical coordinate. The influence of buoyancy on the near-wake fluid dynamics is often small and can be explained by the Richardson number Ri , which is the ratio of buoyancy to flow gradient terms (Lin & Pao, 1979). T_0 is a reference temperature, \bar{T} is the mean temperature, and \bar{U} is the mean velocity. For the single-propeller case, $Ri = g/T_0 (d\bar{T}/dz)/(d\bar{U}/dz)^2 \approx 2.54 \times 10^{-3}$ which means the near-wake inertial forces of the propeller dominate the buoyancy forces. As the local velocity U_x decays, Ri increases and buoyancy forces become important further downstream in the far-wake.

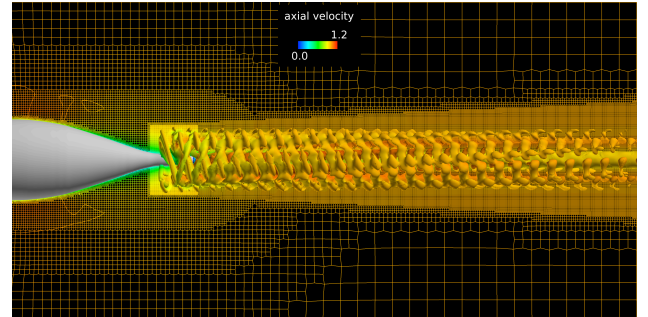
3 RESULTS

3.1 Wake Breakdown

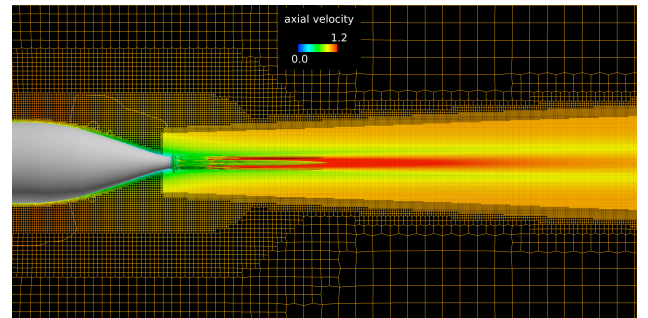
Individual vortices are visualized with the second invariant of the velocity gradient tensor Q . Figure 3 shows contour surfaces of the non-dimensionalized $(L/U_0)^2 Q = 1.7$ with a vertical slice of the mesh colored by axial velocity U_x/U_0 that extends to half of a body-length downstream $x/L = 1.5$. For the single-propeller case, hub- and tip-vortices from the propeller break down by $x/L \approx 1.25$, while for the CRP case, vortical structures persist until $x/L \approx 1.5$. As expected, negligible vortical structures are found in the case of the zero-swirl jet. This figure illustrates the complexity introduced by contra-rotating propellers that delays the formation of a fully-mixed axisymmetric wake profile.



(a) Single propeller.



(b) Contra-rotating propellers.



(c) Jet.

Figure 3: Flow visualization from $1.0 \leq x/L \leq 1.5$ using Q-criterion visualization non-dimensionalized as $(L/U_0)^2 Q = 1.7$ colored by U_x/U_0 .

To better understand the transition from near- to far-wake in the propeller-driven cases, axial planes behind in the wake

are examined. Figure 4 compares the instantaneous and time-averaged axial velocity defect field $U_x/U_0 - 1$. Near the propellers, flow is periodic with the propeller rotation. By half of a body-length downstream, however the flow is stationary in time and space in the body-fixed frame of reference. At $x/L = 1.01$, the instantaneous flow distinguishes individual propeller-blade wakes and varies from that of the time-averaged case. Further downstream at $x/L = 1.2$ a smaller variation is seen, and by $x/L = 1.45$ the two contour maps are nearly identical showing that the wake is steady and revealing a unique hexagonal shape imparted by the CRP. For the single-propeller case, which is not shown, flow is also axisymmetric and steady by $x/L = 1.45$.

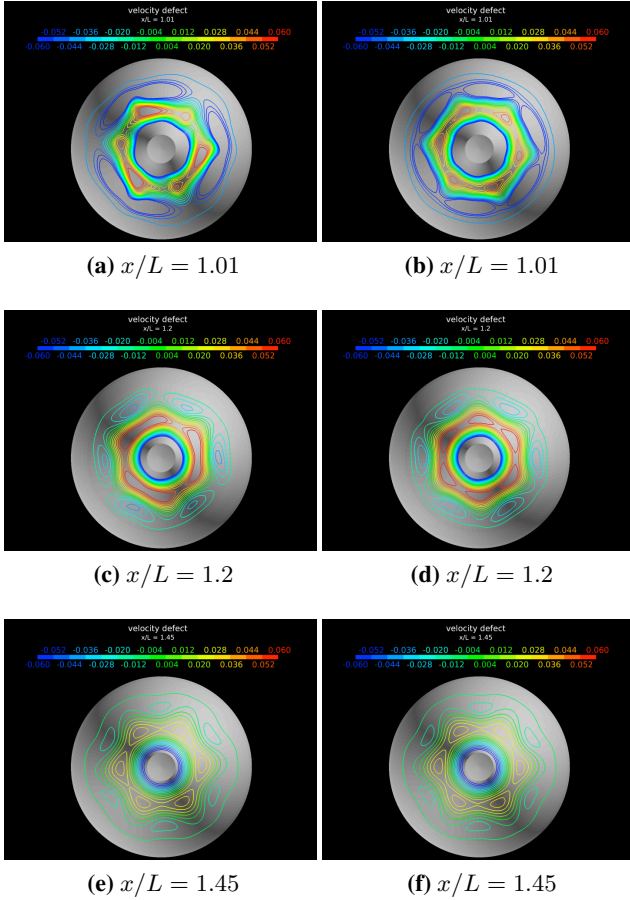


Figure 4: Instantaneous- (ace) and time-averaged- (bdf) velocity-defect field for CRP with $-0.06 \leq U_x/U_0 - 1 \leq 0.06$.

3.2 Velocity Profiles

The evolution of the near-wake may also be described by circumferentially-averaged velocity profiles. Figure 5 shows the circumferentially-averaged axial velocity profiles U_x/U_0 for the three self-propelled configurations at the downstream positions $x/L = 1.01$, $x/L = 1.3$, and $x/L = 1.5$. Just behind the propulsor at $x/L = 1.01$, the jet is shown to have uniform positive velocity leaving the exhaust port, while negative velocity due to drag appears for $r/R_p > 0.2$. By $x/L = 1.3$ and further at $x/L = 1.5$, the jet profile appears as a classical net-zero-momentum wake and may be described using the analytical formula-

tion of the DWCF.

The propeller-driven cases, also net-zero-momentum, show their own unique profiles. Positive momentum from the propellers exists in a lobe at $r/R_p \approx 0.6$, while negative momentum due to drag from the body exists near the center and further outward. These two profiles, when circumferentially averaged, are shown to be nearly-equivalent and decay at similar rates. They also, may be defined analytically using a process described in Jones & Paterson (2016). For all configurations, the positive momentum decays more quickly than the negative momentum, which is a feature of idealized wakes described by Tennekes & Lumley (1972).

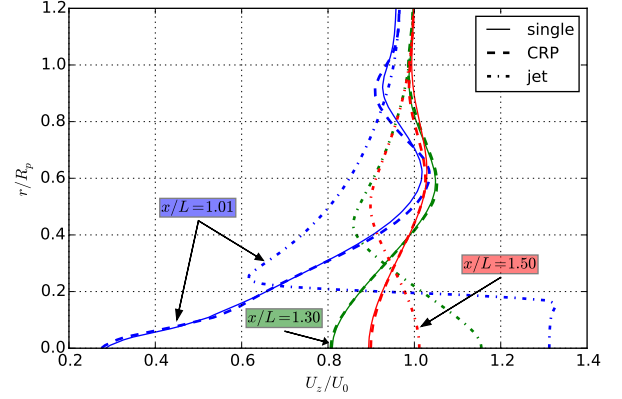


Figure 5: Circumferentially-averaged axial velocity profiles for each configuration at various distances downstream.

Circumferentially averaged profiles of the swirl component of velocity U_θ are shown in Figure 6. The jet exhibits zero-swirl. At $x/L = 1.01$, the single propeller shows the swirl profile due to the propeller and rotating hub. By $x/L = 1.3$ and $x/L = 1.5$, most of the momentum-due-to-swirl exists in a lobe at $r/R_p \approx 0.4$. In the case of the CRP, the swirl is nearly halved in magnitude. Regions of positive and negative swirl develop due to interference between the opposing, contra-rotating blades. Throughout the near-wake, the CRP swirl magnitude is attenuated, remaining less than half of that of the single-propeller.

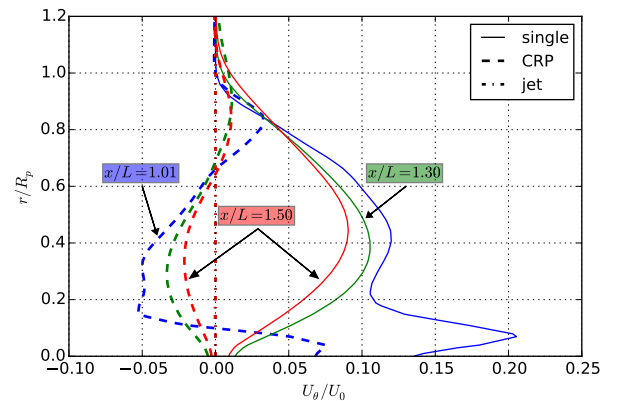


Figure 6: Circumferentially-averaged swirl velocity profiles for each configuration at various distances downstream.

3.3 Mixed-Patch Profiles

3.3.1 Temperature Profiles

By half of a body-length downstream at $x/L = 1.5$, the wake is mixed. Given that the background temperature field was initially linearly stratified, mixing from the wake develops a change-in-temperature field ΔT . This field is non-dimensionalized by the change-in-temperature over the depth of one propeller-blade length ΔT_{R_p} . Figure 7 shows $\Delta T/\Delta T_{R_p}$ for the single-propeller case.

Contours show that a unique profile shape is formed that is steady in time. Colder fluid is driven to the top, while warmer fluid is driven to the bottom of the wake. A nominal mixed-patch profile with uniform- T in the diameter of the wake would look similar, but would not show the “tails” coming off of the hot and cold regions. The direction of the tails is a result of the counter-clockwise swirling motion of the fluid due to the propeller.

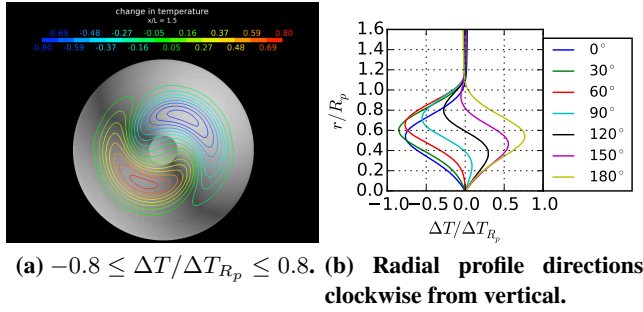


Figure 7: Single propeller $\Delta T/\Delta T_{R_p}$ at $x/L = 1.5$.

The mixed-patch $\Delta T/\Delta T_{R_p}$ profile of the CRP case is shown in Figure 8. Compared to the single-propeller case, the magnitude of $\Delta T/\Delta T_{R_p}$ is less than half. The profile is split between an inner region where clockwise-swirling fluid dominates and an exterior region where counter-clockwise-swirling fluid dominates as shown previously in Figure 6.

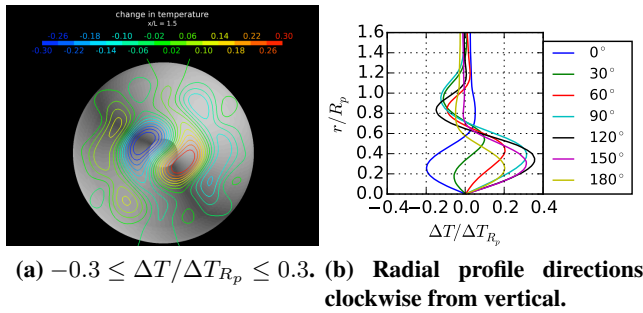


Figure 8: CRP $\Delta T/\Delta T_{R_p}$ at $x/L = 1.5$.

Finally, the mixed-patch $\Delta T/\Delta T_{R_p}$ profile of the jet is shown in Figure 9. For this configuration, the magnitude of $\Delta T/\Delta T_{R_p}$ is the smallest due to the absence of swirl. It is symmetric in both the vertical and horizontal directions. Regions of warmer and colder fluid are focused near the positive-momentum center of the wake, while the negative-momentum periphery shows the reverse in warm and cold regions. Interestingly, the center region

shows warmer fluid above the colder fluid, opposite to the single-propeller profile. This distribution occurs because the positive-momentum center of the wake draws in fluid from the slower-velocity exterior regions, which entrains warmer fluid from above and colder fluid from below.

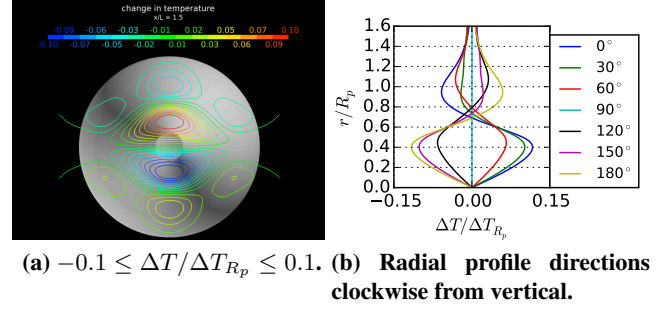


Figure 9: Jet configuration $\Delta T/\Delta T_{R_p}$ at $x/L = 1.5$.

3.3.2 Velocity Profiles

Contour maps of the axial velocity defect $U_x/U_0 - 1$ at $x/L = 1.5$ are shown for the single-propeller and CRP cases in Figure 10. For the single-propeller, axial velocity is axisymmetric and may be fit to an analytical curve as a function of radial distance (Jones & Paterson, 2016). The CRP, however, is not axisymmetric. A steady, hexagonal profile is formed similar in shape to what has been observed in the north polar weather system of Saturn, (Smith et al., 1982, 1981) and later in an experiment using differentially-rotating disks to drive a barotropic jet (Aguiar et al., 2010). Unless circumferentially averaged, this profile may not be described analytically by radius alone.

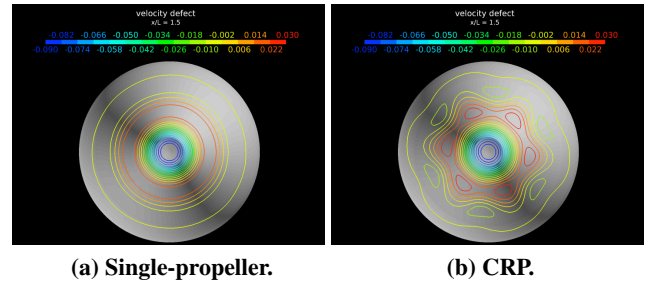


Figure 10: Stationary velocity defect profiles at $x/L = 1.5$ for $-0.09 \leq U_x/U_0 - 1 \leq 0.03$.

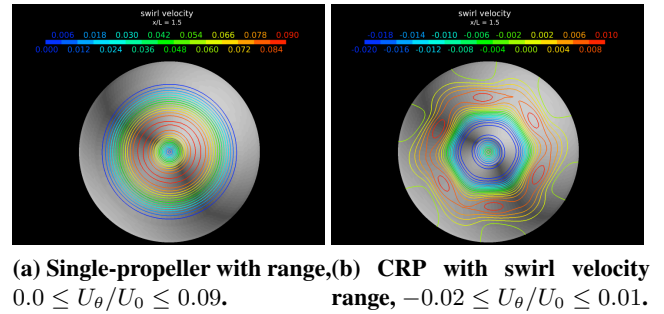


Figure 11: Stationary swirl velocity profiles at $x/L = 1.5$. Note the difference in velocity scale between figures.

The swirl component of velocity U_θ/U_0 is shown in Figure 11. Again, the single-propeller velocity is axisymmetric, while the CRP velocity has discernible geometry. It is important to note the difference in magnitude between the two configurations. Swirl velocity from the CRP is less than that of the single-propeller, and it varies in direction between both clockwise and counter-clockwise.

3.4 Potential and Kinetic Energy Evolution

Kinetic and potential energy is integrated along axial planes downstream for the three configurations as shown in Figure 12. Kinetic energy KE is computed individually for the three components of velocity: radial, swirl, and axial as KE_r , KE_θ , KE_x , as well as the velocity magnitude as total KE. Downstream distance is described both by x/L measured from the bow and by x'/D_p measured from the stern.

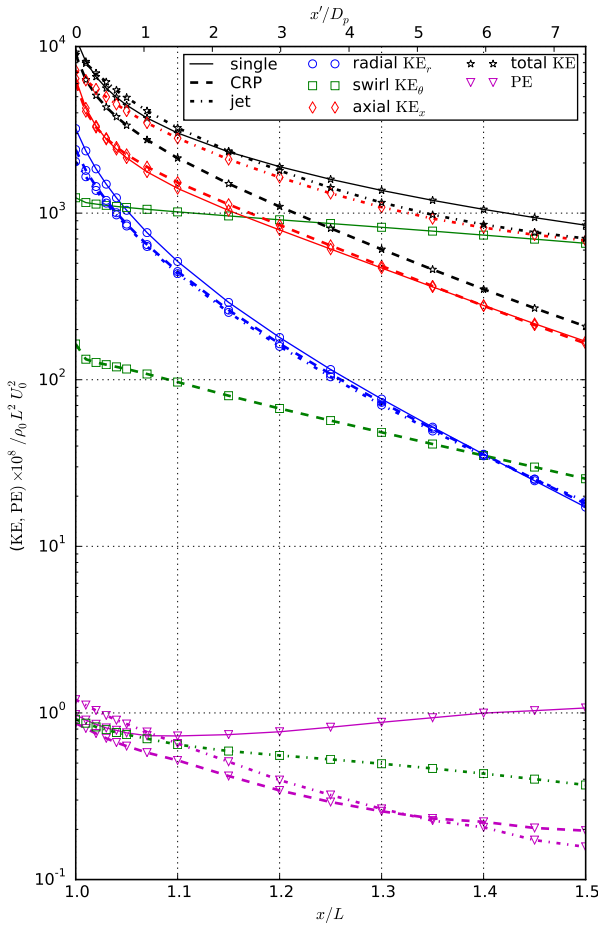


Figure 12: Integrated energy evolution downstream of the vehicle for each configuration, with x measured from the nose of the hull and x' measured from the tail.

For all three cases, KE_r decays more rapidly than KE_x and KE_θ . The swirl component notably decays the slowest demonstrating its persistence in the near-wake. For the single-propeller case, this persistence leads to a rise in PE due to expansion of the wake and entrainment of the surrounding passive scale T . For the CRP, the PE does not

grow due to the opposing azimuthal directions of swirling velocity. Instead the PE decays similar to the zero-swirl jet.

Comparing the swirl component for three cases, KE_θ of the CRP is an order of magnitude lower than that of the single-propeller. The jet KE_θ is several orders of magnitude lower than that. Consequently, the potential energy, seen at the bottom of the chart, is much lower for the CRP than for the single-propeller. This difference in magnitude shows that contra-rotating blades can effectively lower the kinetic energy due to swirl.

Additionally, comparison of the total KE shows that the CRP is the most-effective configuration for total reduction in energy by $x/L = 1.5$. The single-propeller is less effective than the jet due to persisting KE_θ from its unidirectional swirling velocity.

4 CONCLUSIONS

The influence of swirl on the evolution of self-propelled stratified near-wakes is largely unknown. In this study, the near-wake of three propulsor configurations were compared for the appendage-less Iowa Body: single propeller, contra-rotating propellers, and zero-swirl jet. Unsteady, rotating propeller blades were simulated using an AL model in a URANS computation. Visualization of the results showed the helical path of the single-propeller blade-tip vortices as well as the more-complicated vortical structure of the CRP near-wake. Comparison between instantaneous and time-averaged fields indicated that by half of a body length downstream the propeller-driven wakes were mixed and steady. Circumferentially averaged velocity profiles showed the similarities in axial velocity between the single-propeller and CRP. The swirl-velocity magnitude of the CRP was less than half of that of the single-propeller and the swirl profile included regions of both positive and negative swirl. Furthermore, by half of a body-length downstream, mixed-patch contour maps of change-in-temperature demonstrated that the magnitude of $\Delta T/\Delta T_{R_p}$ for the CRP was less than half of that of the single-propeller. The jet $\Delta T/\Delta T_{R_p}$ magnitude was the smallest, due to the absence of meaningful swirl. Contour maps of velocity revealed that the single-propeller has an axisymmetric profile, whereas the CRP exhibits a unique hexagonal structure. Finally integrated energy in downstream axial planes revealed the evolution of kinetic and potential energy in the near-wake. The CRP held an order of magnitude less swirling kinetic energy and potential energy similar in decay and magnitude to that of the swirl-free jet. Additionally, the CRP had the highest decay rate of total kinetic energy.

ACKNOWLEDGMENTS

The first author has been supported by a Rolls-Royce Graduate Fellowship. Virginia Tech Advanced Research Computing is likewise acknowledged for providing high-performance computing resources. Finally, Matt Church-

field is acknowledged for aiding in implementing actuator-line model code from the NREL SOWFA library.

REFERENCES

- Aguiar, A. C. B., Read, P. L., Wordsworth, R. D., Salter, T., & Yamazaki, Y. H. (2010). 'A laboratory model of saturns north polar hexagon'. *Icarus* 206(2): pp. 755–763.
- Brockett, T. (1966). Minimum pressure envelopes for modified naca-66 sections with naca a= 0.8 camber and buships type 1 and type 2 sections. Tech. rep., DTIC Document.
- Brucker, K. A. & Sarkar, S. (2010). 'A comparative study of self-propelled and towed wakes in a stratified fluid'. *Journal of Fluid Mechanics* 652: pp. 373–404.
- Chernykh, G. & Voropayeva, O. (1999). 'Numerical modeling of momentumless turbulent wake dynamics in a linearly stratified medium'. *Computers & fluids* 28(3): pp. 281–306.
- Felli, M., Camussi, R., & Di Felice, F. (2011). 'Mechanisms of evolution of the propeller wake in the transition and far fields'. *Journal of Fluid Mechanics* 682: pp. 5–53.
- Fofonoff, N. P. & Millard, R. C. (1983). 'Algorithms for computation of fundamental properties of seawater'. *Unesco* .
- Hassid, S. (1980). 'Collapse of turbulent wakes in stably stratified media'. *Journal of Hydronautics* 14: pp. 25–32.
- Holliday, D. & McIntyre, M. E. (1981). 'On potential energy density in an incompressible, stratified fluid'. *Journal of Fluid Mechanics* 107: pp. 221–225.
- Hyun, B. S. (1990). Measurements in the flow around a marine propeller at the stern of an axisymmetric body. Ph.D. thesis, University of Iowa, Iowa City, Iowa.
- Hyun, B. S. & Patel, V. C. (1991). 'Measurements in the flow around a marine propeller at the stern of an axisymmetric body'. *Experiments in Fluids* 11(1): pp. 33–44.
- Jones, M. C. & Paterson, E. G. (2016). 'Evolution of the propeller near-wake and potential energy in a thermally-stratified environment'. *Proceedings of OCEANS 2016 MTS/IEEE Monterey* pp. 1–10.
- Lin, J. & Pao, Y. (1974). 'Velocity and density measurements in the turbulent wake of a propeller-driven slender body in a stratified fluid'. *Flow Research Inc* .
- Lin, J. & Pao, Y.-H. (1979). 'Wakes in stratified fluids'. *Annual Review of Fluid Mechanics* 11(1): pp. 317–338.
- Lucca-Negro, O. & O'Doherty, T. (2001). 'Vortex breakdown: a review'. *Progress in energy and combustion science* 27(4): pp. 431–481.
- Martinez, L. A., Leonardi, S., Churchfield, M. J., & Moriarty, P. J. (2012). 'A comparison of actuator disk and actuator line wind turbine models and best practices for their use'. *AIAA Paper* (2012-0900).
- Menter, F. R. (1994). 'Two-equation eddy-viscosity turbulence models for engineering applications'. *AIAA journal* 32(8): pp. 1598–1605.
- Meunier, P. & Spedding, G. R. (2006). 'Stratified propelled wakes'. *Journal of Fluid Mechanics* 552: pp. 229–256.
- Naudascher, E. (1965). 'Flow in the wake of self-propelled bodies and related sources of turbulence'. *Journal of Fluid Mechanics* 22(04): pp. 625–656.
- Sanderse, B., Pijl, S., & Koren, B. (2011). 'Review of computational fluid dynamics for wind turbine wake aerodynamics'. *Wind Energy* 14(7): pp. 799–819.
- Schetz, J. & Jakubowski, A. (1975). 'Experimental studies of the turbulent wake behind self-propelled slender bodies'. *AIAA Journal* 13(12): pp. 1568–1575.
- Sirviente, A. & Patel, V. C. (2000a). 'Wake of a self-propelled body, part 1: Momentumless wake'. *AIAA journal* 38(4): pp. 613–619.
- Sirviente, A. & Patel, V. C. (2000b). 'Wake of a self-propelled body, part 2: Momentumless wake with swirl'. *AIAA journal* 38(4): pp. 620–627.
- Smith, B. A., Soderblom, L., Batson, R., Bridges, P., Inge, J., Masursky, H., Shoemaker, E., Beebe, R., Boyce, J., Briggs, G. et al. (1982). 'A new look at the saturn system: The voyager 2 images'. *Science* 215(4532): pp. 504–537.
- Smith, B. A., Soderblom, L., Beebe, R., Boyce, J., Briggs, G., Bunker, A., Collins, S. A., Hansen, C. J., Johnson, T. V., Mitchell, J. L. et al. (1981). 'Encounter with saturn: Voyager 1 imaging science results'. *Science* 212(4491): pp. 163–191.
- Tennekes, H. & Lumley, J. L. (1972). A first course in turbulence. MIT press.
- Troldborg, N. (2008). Actuator Line Modeling of Wind Turbine Wakes. Ph.D. thesis, Technical University of Denmark, Lyngby, Denmark.